RESEARCH ARTICLE

ATMOSPHERIC PHYSICS

Substantial convection and precipitation enhancements by ultrafine aerosol particles

Jiwen Fan,[1]* Daniel Rosenfeld,[2] Yuwei Zhang,[1,3] Scott E. Giangrande,[4] Zhanqing Li,[3,5] Luiz A. T. Machado,[6] Scot T. Martin,[7] Yan Yang,[1,8] Jian Wang,[4] Paulo Artaxo,[9] Henrique M. J. Barbosa,[9,10] Ramon C. Braga,[6] Jennifer M. Comstock,[1] Zhe Feng,[1] Wenhua Gao,[1,11] Helber B. Gomes,[12] Fan Mei,[1] Christopher Pöhlker,[13] Mira L. Pöhlker,[13] Ulrich Pöschl,[13,14] Rodrigo A. F. de Souza[15]

Aerosol-cloud interactions remain the largest uncertainty in climate projections. Ultrafine aerosol particles smaller than 50 nanometers ($UAP_{<50}$) can be abundant in the troposphere but are conventionally considered too small to affect cloud formation. Observational evidence and numerical simulations of deep convective clouds (DCCs) over the Amazon show that DCCs forming in a low-aerosol environment can develop very large vapor supersaturation because fast droplet coalescence reduces integrated droplet surface area and subsequent condensation. $UAP_{<50}$ from pollution plumes that are ingested into such clouds can be activated to form additional cloud droplets on which excess supersaturation condenses and forms additional cloud water and latent heating, thus intensifying convective strength. This mechanism suggests a strong anthropogenic invigoration of DCCs in previously pristine regions of the world.

Deep convective cloud (DCC) systems in the tropics produce copious precipitation and drive the global-scale circulation (*1*). Precipitation, latent heating, and cloud radiative forcing associated with DCCs are strongly modulated by cloud microphysical processes (*2*). These processes in tropical DCCs are initiated from droplet nucleation (which is determined by vapor supersaturation in updrafts and aerosol properties such as composition and size distribution. Aerosol impacts on cloud processes via this pathway are known as aerosol indirect effects, referred to as aerosol-cloud interaction in the most recent Intergovernmental Panel on Climate Change report (*3*). Aerosol impacts are a key uncertainty in understanding the current and future climate (*3*) as well as extreme weather (*4*). DCCs have complicated dynamics and microphysics; therefore, aerosol impacts on them are extremely complex and hard to disentangle. Previous studies have shown that aerosols could invigorate or suppress DCC intensity through aerosol indirect effects, contingent on dynamical and thermodynamical conditions [e.g., (*4*–*12*)]. In the case of warm-cloud bases (>15°C), increasing aerosol concentrations can suppress warm rain because of a reduction in droplet size, which allows more cloud water to be lifted to a higher altitude; the freezing of this larger amount of cloud water releases additional latent heat, thereby invigorating convective updrafts [referred to as "cold-phase invigoration" (*13*)]. The importance of the process of enhanced condensation by aerosols to deep-cloud development has been shown in tropical maritime clouds (*14*–*16*). Enhancement in DCC intensity favors enhanced storm electrification, larger precipitation rates, and taller clouds with larger anvils.

Over the Amazon, unperturbed background aerosol concentrations found within the region of pristine rainforests are low, with values reported in the low hundreds per cubic centimeter (*17*–*19*), similar to conditions thought to have existed in preindustrial times (*18*). Responses of cloud properties to aerosols are nonlinear and most sensitive to the addition of particles when the background concentration is very low [i.e., the "aerosol-limited regime" (*17*, *20*, *21*)]. Therefore, the aerosol effect on convective clouds over the Amazon region is expected to be large, and previous studies have demonstrated evident smoke aerosol influence on convective clouds during dry seasons in the Amazon (June to September) (*22*–*24*). In addition to the low total aerosol concentration, ultrafine aerosol particles with diameters less than 50 nm ($UAP_{<50}$) are typically nearly absent over the Amazon rainforest, as new particle formation has rarely been observed in the boundary layer there (*25*, *26*). $UAP_{<50}$ are often transported downward from the upper troposphere and subsequently grow to the particles larger than 50 nm that are traditionally considered as cloud condensation nuclei ($CCN_{>50}$) (*27*). However, the Manaus metropolis, a city of about 2 million people, produces a pollution plume that generally follows the northeasterly trade winds and is an important source of elevated $UAP_{<50}$ concentrations (*28*).

The Observations and Modeling of the Green Ocean Amazon (GoAmazon 2014/5) experiment was carried out near the Manaus metropolis to gain a better understanding of the impacts of pollution emissions from Manaus on the hydrological cycle and climate in the tropical rainforest (*29*, *30*). We took advantage of the unique observational data from GoAmazon 2014/5 (e.g., the direct cloud updraft velocity measurements for DCCs occurring in a similar convective environment but different aerosol environment) to investigate the observed aerosol effects, as well as to perform and analyze high-resolution simulations of a sample case, using the detailed spectral-bin microphysics scheme to scrutinize the mechanism. We found that the $UAP_{<50}$ introduced by the Manaus pollution plume enhanced convective intensity and precipitation rates to a degree not previously observed or simulated. The detailed simulations show that the drastic enhancement in convective intensity is primarily attributable to the enhanced condensational heating, with the latent heat released from enhanced ice-related processes at upper levels playing a secondary role. This differs from the previous "cold-cloud invigoration" concept (*13*), which does not consider aerosol impacts on condensational heating. As illustrated in Fig. 1, the enhanced condensational heating is driven mainly by the activation of $UAP_{<50}$ well above the cloud base, which is attributable to high vapor supersaturation with respect to water (S_w) resulting from fast droplet coalescence. The subsequent condensational growth considerably lowers the water supersaturation, liberating additional latent heating in the lower atmosphere, which enhances convective intensity drastically. The additional condensate from this process increases the amounts of both warm rain and supercooled cloud water. Furthermore, enhanced droplet freezing, including riming, occurs as a result of the production of additional supercooled water, and intensified convection enhances ice deposition at high levels.

---

[1] Atmospheric Sciences and Global Change Division, Pacific Northwest National Laboratory, Richland, WA 99352, USA. [2] Institute of Earth Sciences, Hebrew University of Jerusalem, Jerusalem 91904, Israel. [3] Department of Atmospheric and Oceanic Science and ESSIC, University of Maryland, College Park, MD 20742, USA. [4] Environmental and Climate Sciences Department, Brookhaven National Laboratory, Upton, NY, USA. [5] State Laboratory of Earth Surface Process and Resource Ecology, GCESS, Beijing Normal University, Beijing, China. [6] Centro de Previsão de Tempo e Estudos Climáticos, Instituto Nacional de Pesquisas Espaciais, Cachoeira Paulista, Brazil. [7] School of Engineering and Applied Sciences and Department of Earth and Planetary Sciences, Harvard University, Boston, MA, USA. [8] Beijing Municipal Weather Modification Office, Beijing 100089, China. [9] Instituto de Física, Universidade de São Paulo, Rua do Matão 1371, 05508-090 São Paulo, Brazil. [10] Department of Physics, University of Maryland Baltimore County, Baltimore, MD, USA. [11] State Key Laboratory of Severe Weather, Chinese Academy of Meteorological Sciences, Beijing 100086, China. [12] Atmospheric and Climate Dynamics Laboratory, Institute of Atmospheric Sciences, Federal University of Alagoas, Brazil. [13] Multiphase Chemistry and Biogeochemistry Departments, Max Planck Institute for Chemistry, 55020 Mainz, Germany. [14] Johannes Gutenberg University Mainz, 55122 Mainz, Germany. [15] Department of Meteorology, School of Technology, Amazonas State University (UEA), Manaus-AM, Brazil.
*Corresponding author. Email: jiwen.fan@pnnl.gov

Cumulatively, these enhanced ice-related processes at middle and upper levels further enhance convection, but to a much lesser degree relative to enhanced condensation at low levels. The effects of $\mathrm{UAP}_{<50}$ contrast with those of $\mathrm{CCN}_{>50}$: $\mathrm{UAP}_{<50}$ increase warm rain rate and have no effect on the timing of peak rain rate, whereas $\mathrm{CCN}_{>50}$ suppress warm rain rate and delay the timing of peak rain rate.

Observed relationships of convective intensity and precipitation with aerosols

The measurements from the U.S. Department of Energy (DOE) Atmospheric Radiation Measurement 1290-MHz Ultra High Frequency (UHF) Radar Wind Profilers [RWP (*31*, *32*)] during GoAmazon 2014/5 provide the most accurate data on vertical air motions and precipitation rates for Amazon DCCs, allowing us to directly examine the relationship of updraft intensity to aerosols. We focused on convective cells of local origin (*33*, *34*), favoring relatively simple and similar dynamics across such DCCs in the wet season. The intrusion of the Manaus pollution plume provides a natural laboratory for exploring pollution aerosol effects. Our analysis period was the 2014 wet season (1 March to 31 May). Figure 2 shows the correlation of mean vertical velocity estimated for the top 10th percentile of updrafts in each convective event with the respective aerosol particle number concentration (N_a), averaged over a 30-min period before the start of convection at the T3 site (~70 km southwest of Manaus, downwind). The N_a at the T3 site varied substantially from case to case. We found that convective updraft velocity (w) increased with an increase of N_a for aerosols with a diameter (D) larger than 15 nm (Fig. 2A, top). When the updraft velocity was segregated according to four aerosol groups (ranging from lower to higher N_a), we observed a monotonic and striking increase of w, which increased from 4 m s^{-1} for the lowest-N_a group to 10 m s^{-1} for the highest-N_a group (Fig. 2B, left). The corresponding radar reflectivity (a measure of precipitation intensity) also increased with increasing N_a throughout the vertical profile for D > 15 nm (Fig. 2C, left), associated with hydrometeor size and precipitation rate increases. Remarkably, the increasing trend in updraft intensity and radar reflectivity as N_a increases does not hold well when considering only those aerosols with D > 50 nm (Fig. 2A, bottom, and Fig. 2B, right; similar results were obtained for D > 100 nm). The result suggests that $\mathrm{UAP}_{<50}$, not $\mathrm{CCN}_{>50}$, are the primary drivers for intensified convection. The probability density functions of w and rain rate from the four aerosol groups indicate that occurrences of stronger updraft velocities are more frequent with the increase of N_a for $\mathrm{UAP}_{<50}$ (fig. S1A, left) and that the maximum rain rates also increase (fig. S2C).

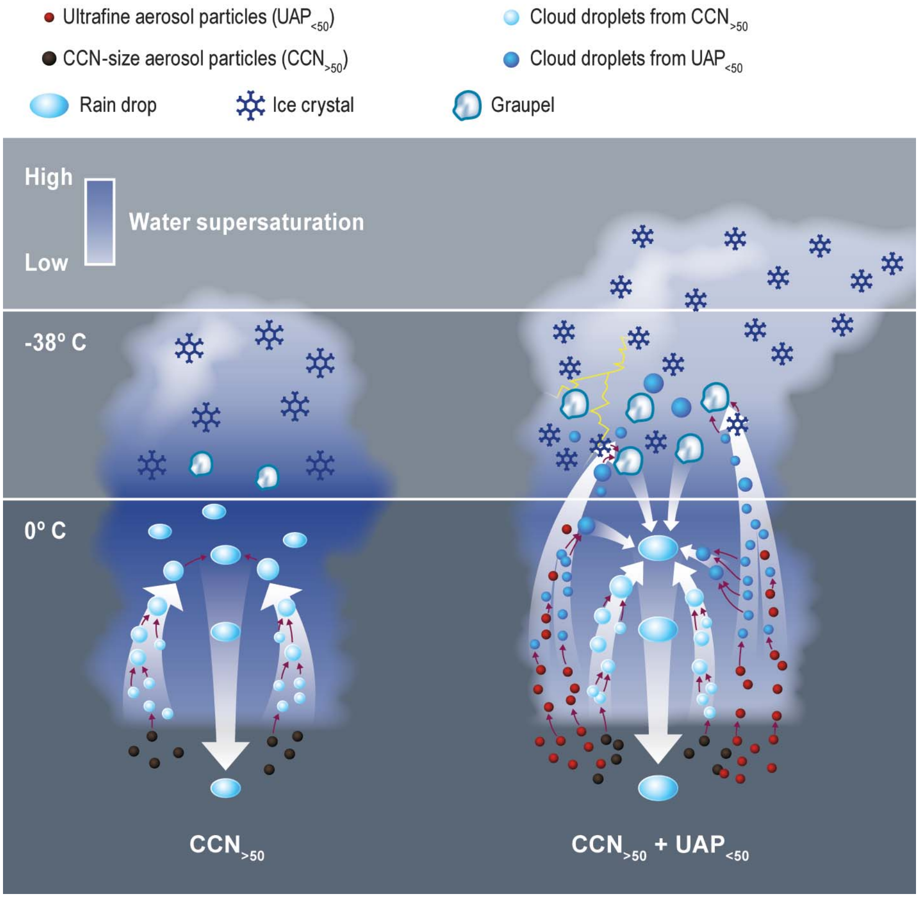

Fig. 1. Illustration of the effect of ultrafine aerosol particles ($\mathrm{UAP}_{<50}$) on tropical convective clouds. In clouds that lack $\mathrm{UAP}_{<50}$ (left), the clouds are highly supersaturated as a result of fast drop coalescence that forms warm rain and reduces the integrated droplet surface area available for condensation. With added $\mathrm{UAP}_{<50}$ (right, red dots), an additional number of cloud droplets are nucleated above cloud base, which lowers supersaturation drastically by enhanced condensation, releasing additional latent heat at low and middle levels, thus intensifying convection. The additional condensate adds to both the warm rain and supercooled cloud water; when freezing occurs aloft, this addition further enhances convection (i.e., a small increase in convection but enhancement of precipitation and storm electrification).

To corroborate that $\mathrm{UAP}_{<50}$ are the main factor contributing to the observed DCC enhancements, we conducted additional analyses to help isolate aerosol effects from thermodynamic controls. Locally driven Amazon deep convective events within the wet season should initiate and evolve under similar diurnal controls on their dynamical and thermodynamical environments (*33*, *35*). We examined traditional radiosonde thermodynamic forcing parameters such as the convective available potential energy (CAPE) and convective inhibition (CIN) before convection. The CAPE is very similar for these events (Fig. 2A, black circles) and is not strongly correlated with updraft intensity. Under similar CAPE conditions, CIN magnitudes should help to reveal how likely it is for DCCs to initiate and to determine what may be their relative intensities. CIN varies quite a bit (Fig. 2A, triangles) but again shows no correlation with the enhanced convective intensity as N_a of $\mathrm{UAP}_{<50}$ increases. Analyses of profiles of the temperature, relative humidity (RH), and zonal U- and meridional V-components of the wind fields representative of the pre-storm environment also indicate that these environmental profiles do not correlate with an increase of updraft intensity as N_a of $\mathrm{UAP}_{<50}$ increases (fig. S3). In fact, our lowest-N_a group exhibited higher RH at 2- to 5-km altitudes than did the higher-N_a groups, which should have favored stronger convection and offset some aerosol effects. This means that the trend for enhanced updraft intensity with the increase of N_a counting $\mathrm{UAP}_{<50}$ should have potentially been more prominent if RH for the lowest-N_a group is similar to those of the higher-N_a groups. Although we cannot guarantee that RWP observations captured the representative updraft cores for every single event, these analyses do not show any covariation of aerosols with dynamics and thermodynamics for these locally occurring systems. This provides clear evidence that the enhanced convective intensity seen with the increase in N_a of $\mathrm{UAP}_{<50}$ is not solely controlled by factors other than $\mathrm{UAP}_{<50}$.

Modeled mechanism

To understand the physical processes and mechanisms responsible for the observed intensification of updrafts by $\mathrm{UAP}_{<50}$, we conducted model simulations at a cloud-resolving scale of 0.5 km for a typical wet season convective event, as on 17 March

2014 (fig. S4) (*34*). We used detailed spectral-bin microphysics (*36*, *37*) coupled with the Weather Research and Forecasting model (*38*). The simulation for the observed case ("baseline") is P3_BG, using a value of 950 cm^{-3} (130 $CCN_{>50}$ + 820 $UAP_{<50}$) for the present-day background aerosol concentration; the concentration in the Manaus metropolis (fig. S5B, black box) was set to be higher by a factor of 3 for both $CCN_{>50}$ and $UAP_{<50}$ to account for the effect of the Manaus pollution plume (Table 1). The aerosol size distribution (SD) is shown in fig. S5C. The power-law SD for $UAP_{<50}$ followed the observed shape in the city of Manaus (fig. S6C, line 1). For $CCN_{>50}$ (D > 50 nm), the SD is based on data from a remote rainforest site known as the Amazon Tall Tower Observatory (ATTO) in the central Amazon Basin (*39*, *40*), approximating a clean preindustrial (PI) condition (C_PI). C_BG is the simulation based on P3_BG, except with the Manaus pollution plume removed. To explore the effects of $UAP_{<50}$, we performed another pair of simulations, C_PI and PL3_PI, based on C_BG and P3_BG (Table 1), respectively, except with $UAP_{<50}$ removed (fig. S5C). Therefore, C_PI represents the PI condition without $UAP_{<50}$. The vertical distribution (VD) is shown in fig. S6A, and the details are in (*34*). Besides the four main simulations used to demonstrate the mechanism and isolate the contributions, we also conducted sensitivity tests (Table 1) with a different aerosol VD (C_BG_VD and C_PI_VD) and SD (P3_BG_SD, C_BG_SD, and C_PI_SD) to examine how the proposed mechanism is affected by variously measured aerosol properties. The sensitivity test C_PI2 was intended to show that the results do not change qualitatively even if a small amount of $UAP_{<50}$, as observed in the pristine condition over the Amazon, exists (*34*).

We evaluated the baseline simulation (P3_BG) with available observations (figs. S7 to S9) (*34*). Overall, the simulation is in good agreement with the observed case in terms of profiles of temperature, water vapor, and wind fields (fig. S7); the precipitation rate and the timing of peak precipitation (figs. S8 and S9A); and the echo-top heights of 10 dBZ (fig. S9B). These observational metrics provide confidence in the model performance.

With the sensitivity tests based on the baseline simulation, we found that adding $UAP_{<50}$ to the PI environment without $UAP_{<50}$ markedly invigorates convective intensity (Fig. 3A, C_PI versus C_BG and PL3_PI versus P3_BG). The probability density functions of updraft velocity clearly convey the same point (fig. S10). Therefore, the model replicates results that were observed: $UAP_{<50}$, which are abundant in the Manaus pollution plume, lead to enhanced convection around the T3 area. The convective intensity is more than 50% weaker in the PI environment (C_PI) when compared to the perturbed environment by the urban plume (P3_BG). As a result, the peak rain rate is greater by a factor of nearly 2.5 (Fig. 3C). Even under the present-day Manaus regional background condition that already contains an appreciable amount of $UAP_{<50}$ (820 cm^{-3}), further increasing $UAP_{<50}$ due to the Manaus pollution plume by a factor of 3 still drastically enhances convective intensity (by about 40%) in the downwind area (P3_BG versus C_BG). The corresponding increase in the peak precipitation rate is nearly 100%, much more substantial than that of convective intensity. This result highlights the ubiquity of convective invigoration by aerosols in Amazonia (i.e., in both PI and present-day Manaus regional background environments) and the nonlinear response of precipitation rates to convective intensity. The ubiquity of convective invigoration by the Manaus pollution plume is also corroborated by much more frequent strong updrafts over the entire domain from C_PI to C_BG

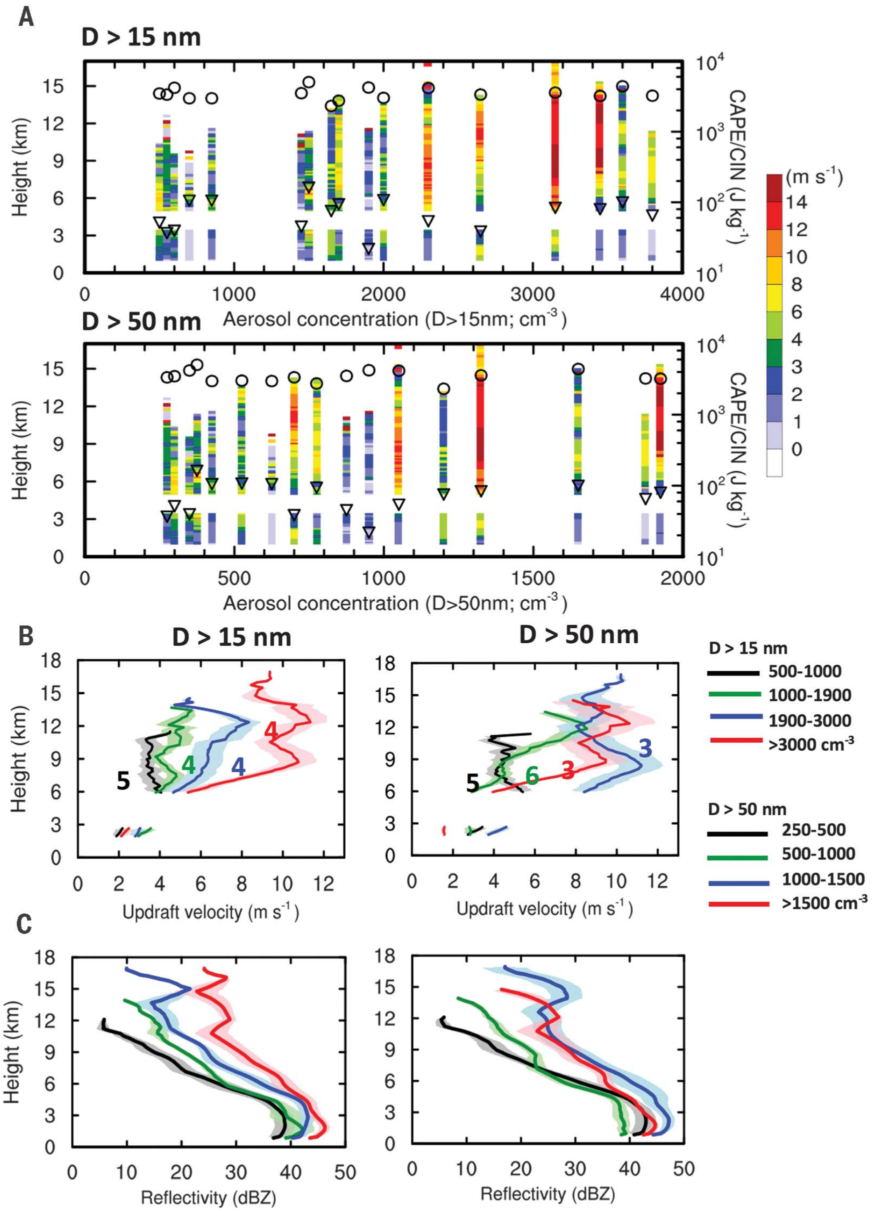

Fig. 2. Observed updraft velocity (*w*) and radar reflectivity (Z_e) as aerosol increases. (**A**) Vertical profiles of updraft velocity averaged over the 90th to 100th percentile of updrafts in each selected local convective case as a function of N_a with D > 15 nm (top) and D > 50 nm (bottom). Each profile column represents one case. The circles and triangles denote the CAPE and CIN values of each case, respectively. The aerosol value for each case is listed in table S1. (**B**) Vertical profiles of the updraft velocity averaged over the top 10 percentiles of updrafts for each case for the four aerosol groups from lower to higher N_a for D > 15 nm (left) and D > 50 nm (right). The number of cases for each group is marked. (**C**) Same as (B) except for reflectivity. Values of (B) and (C) are the means of the collection of the top 10 percentiles of updrafts from each case. The top 10 percentiles of the updrafts have 20 to 40 data points for most of the vertical levels and a few for some high levels in each case. The data have a vertical resolution of ~120 m and time resolution of ~6 s. Shaded areas in (B) and (C) represent the standard error of the data.

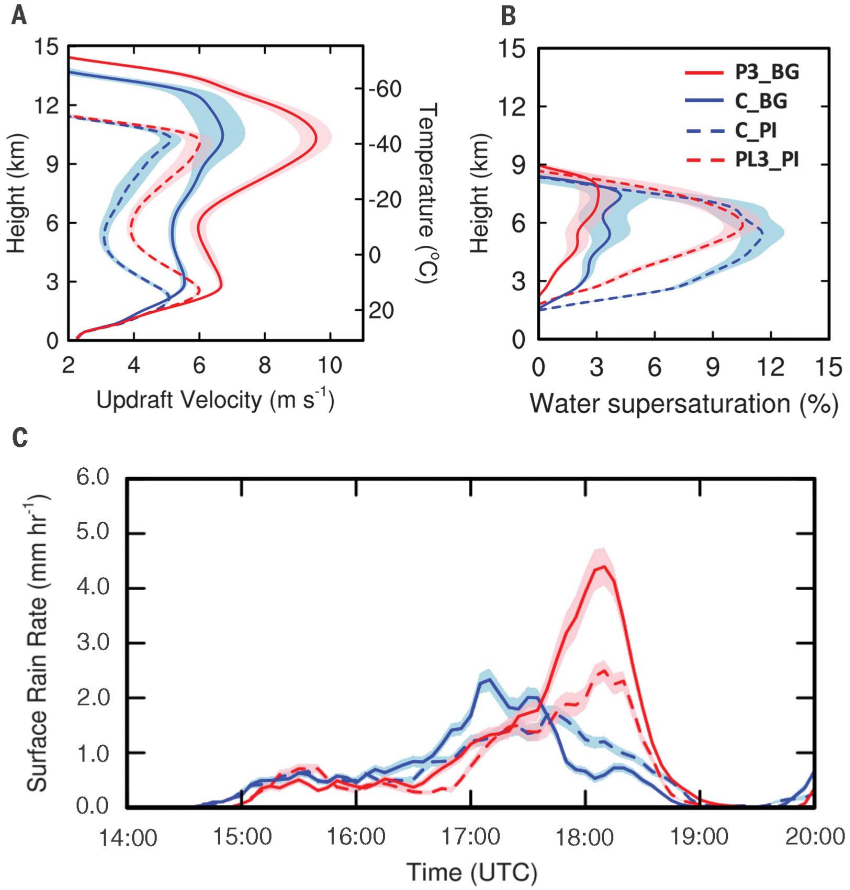

Fig. 3. Simulated aerosol effects on the DCCs. (**A** and **B**) Vertical profiles of updraft velocity w (A) and water supersaturation (B) averaged over the top 10 percentiles (i.e., 90th to 100th) for the updrafts with $w > 2$ m s^{-1} during 1400–1900 UTC from the convective clouds around the T3 site (red box in fig. S8). (**C**) Time series of mean surface rain rate averaged over the red box area from simulations of C_PI (blue dashed curve), C_BG (blue solid curve), PL3_PI (red dashed curve), and P3_BG (red solid curve). The right-side y axis in (A) shows the temperature profile. The convective clouds over T3 were chosen for analysis because they are affected by the Manaus pollution plume in P3_BG and evaluated by observations as shown in figs. S7 to S9. Comparisons with radar-retrieved rain rates at 2.5-km altitude are shown in figs. S8 and S9A. Shaded areas represent the standard error of the data.

(fig. S11). Another notable feature is that the timing of the peak rain rate is delayed when increasing CCN$_{>50}$, consistent with previous studies. However, adding UAP$_{<50}$ to the same CCN condition does not change the timing, although it greatly enhances the rain rate resulting from enhanced convective intensity. The reason for no change in the timing of rain by UAP$_{<50}$ is discussed later.

Further analysis shows that the mechanism responsible for such strongly enhanced convective intensity by UAP$_{<50}$ is different from the "cold-phase invigoration" previously proposed (*13*). We used comparisons between C_PI and C_BG to demonstrate our proposed mechanism (similar conclusions were drawn from comparisons between PL3_PI and P3_BG). The warm- and deep-cloud periods were examined. The vertical velocity increase under the deep-cloud period correlates with the increase in total buoyancy (no correlation with cold pool intensity is seen), although the condensate loading effect partially offsets the thermal buoyancy (Fig. 4B, bottom). The thermal buoyancy increase is attributed to the increased net latent heating (fig. S12A).

Next, we detail how latent heating is increased and which microphysical processes are the major contributors. In the PI environment (C_PI), for the warm-cloud period after warm rain initiates, the mean S_w for the top 10th percentile of updrafts can be nearly 4% (Fig. 4A, top) because of the efficient warm rain formation due to fast droplet coalescence resulting from large droplet size, which reduces the integrated droplet surface area for condensation (Fig. 5A, top). The addition of UAP$_{<50}$ (C_BG) brings the S_w down to 1%, because UAP$_{<50}$ form an additional number of droplets above the cloud base—a result of smaller critical aerosol size for activation under high S_w (Fig. 4A, second from top). These droplets increase the integrated surface area above the cloud base by more than 40% (Fig. 5A, top) and therefore promote condensational growth even at the warm-cloud period (Fig. 4A, third from top). Note that enhanced condensation leads not only to the increased cloud water but also to a rainwater increase under the warm-cloud period (Fig. 5A, bottom). This result is corroborated by aircraft measurements of warm clouds during GoAmazon2014/5, showing larger liquid water content in the plume-affected clouds relative to background clouds; enhanced condensation efficiency is part of the explanation (*41*). Under the deep-cloud period, the condensation effect is further amplified; the S_w reaches up to 15% in C_PI because of a lack of droplet surface area for condensation and decreases to 7% in C_BG (Figs. 4B and 5B, top). This allows aerosols as small as 10 nm to be activated into cloud droplets (Fig. 4B, second from top). The activation of UAP$_{<50}$ leads to a factor of 2 to 4 increase of the integrated droplet surface area and a doubled condensational heating rate (Fig. 4B, third from top). The decrease of supersaturation by UAP$_{<50}$ is similarly evident even over the entire convective period 1400–1900 UTC (Fig. 3B).

Because of the very small critical size for droplet nucleation at 2.5- to 3-km altitude, another droplet nucleation peak appears above the peak at the cloud base in C_BG; this is attributable to the presence of a large amount of UAP$_{<50}$ (Fig. 4B, top, pink solid line). Without UAP$_{<50}$, cloud droplet nucleation occurs predominantly at the cloud base because almost all of the aerosol particles can be activated there (Fig. 4B, top, pink dashed line). The addition of UAP$_{<50}$ makes droplet nucleation occur at a large rate above the cloud base and up to an altitude of 8 km as a result of transport of UAP$_{<50}$ from low levels. The enhanced droplet nucleation over the vertical profile from C_PI to C_BG leads to an increase of up to a factor of 2 to 3 in condensational heating occurring throughout the lower and middle troposphere. The magnitude of condensational heating in C_BG is nearly twice that of depositional heating, indicating the predominance of the condensation process in the release of latent heat. The increase in depositional heating from C_PI to C_BG is also much less than that of condensational heating and is only located at 10- to 12-km altitude, whereas condensational heating is located at low and middle levels and has a deep layer of increase. The latent heating rates from riming and drop freezing increase considerably from C_PI to C_BG as well. The increases in drop freezing and riming rates result from the transport of additional droplets from low levels. Although the increasing rate in latent heating from drop freezing is the largest, the actual magnitude is too small (relative to the other processes) for latent heat to play an important role. The latent heat from riming is also substantially smaller than that from condensation and deposition.

To understand the relative role of the enhanced condensational heating and latent heating from ice-related processes in intensifying convection, we conducted three sensitivity tests based on P3_BG (*34*). These tests show that enhanced condensational heating is the predominant player in the intensification of convection and precipitation, while enhanced latent heating at upper levels plays a secondary role (figs. S13 and S14). This is different from "cold-phase invigoration" (i.e., enhanced ice-related processes), which is caused by the addition of CCN that can be activated at the cloud base via suppressing coalescence and delaying warm rain. $UAP_{<50}$ do not suppress the initial droplet coalescence and delay the rain, because $UAP_{<50}$ can only be activated above the cloud base when rain has already formed and supersaturation is enhanced by a reduced droplet surface area available for condensation. Although previous idealized simulations suggested that smaller aerosol particles can enhance DCC intensity through condensational heating (*14*), our observations and simulations show that it actually occurs and has surprisingly large magnitude and importance.

Because of this greatly enhanced convection associated with $UAP_{<50}$, the mass mixing ratios of all hydrometeors are nearly doubled under the deep-cloud period (Fig. 5B, bottom). The activation of $UAP_{<50}$ leads to an increase—up to an order of magnitude—in droplet number concentrations (Fig. 5B, middle), as well as a drastic increase in ice-phase particle concentrations resulting from enhanced freezing including riming. All ice-phase particle number concentrations (ice, snow, and graupel) increase by a factor of ~2 generally, but the increase of the mass mixing ratio of ice-phase particles is largely driven by graupel, with snow mass reduced (fig. S12B, left), particularly in mixed-phase regions (6 to 10 km), resulting from a larger amount of supercooled liquid droplets in the cases of $UAP_{<50}$. Falling graupel particles contribute to warm-phase increases in rain mass under the deep-cloud period (Fig. 5B, bottom), thereby contributing to increased surface precipitation as in Fig. 3C.

Summary and discussion

The retrieved updraft velocity from RWP has allowed us to directly examine and constrain aerosol impacts on updraft intensity for DCCs occurring in a similar dynamic and thermodynamic environment except for aerosols, revealing the potentially substantial convective updraft and precipitation enhancements by $UAP_{<50}$ from the Manaus pollution plume. We used real-case three-dimensional simulations to reproduce observed convective cloud characteristics and to observe convective updraft and precipitation enhancements by $UAP_{<50}$ over the Amazon region. The physical mechanism for such strong intensification of convection stems from the strong capacity of these DCCs in activating $UAP_{<50}$ that usually have a much higher number concentration than $CCN_{>50}$, because fast droplet coalescence in pristine conditions decreases integrated droplet surface area for condensational growth, producing highly supersaturated conditions. The subsequent condensational growth of an additional number of droplets considerably lowers the water supersaturation, liberating a large amount of additional latent heat at the low and middle levels of DCCs and considerably enhancing updraft strength. This "warm-phase invigoration" has much stronger

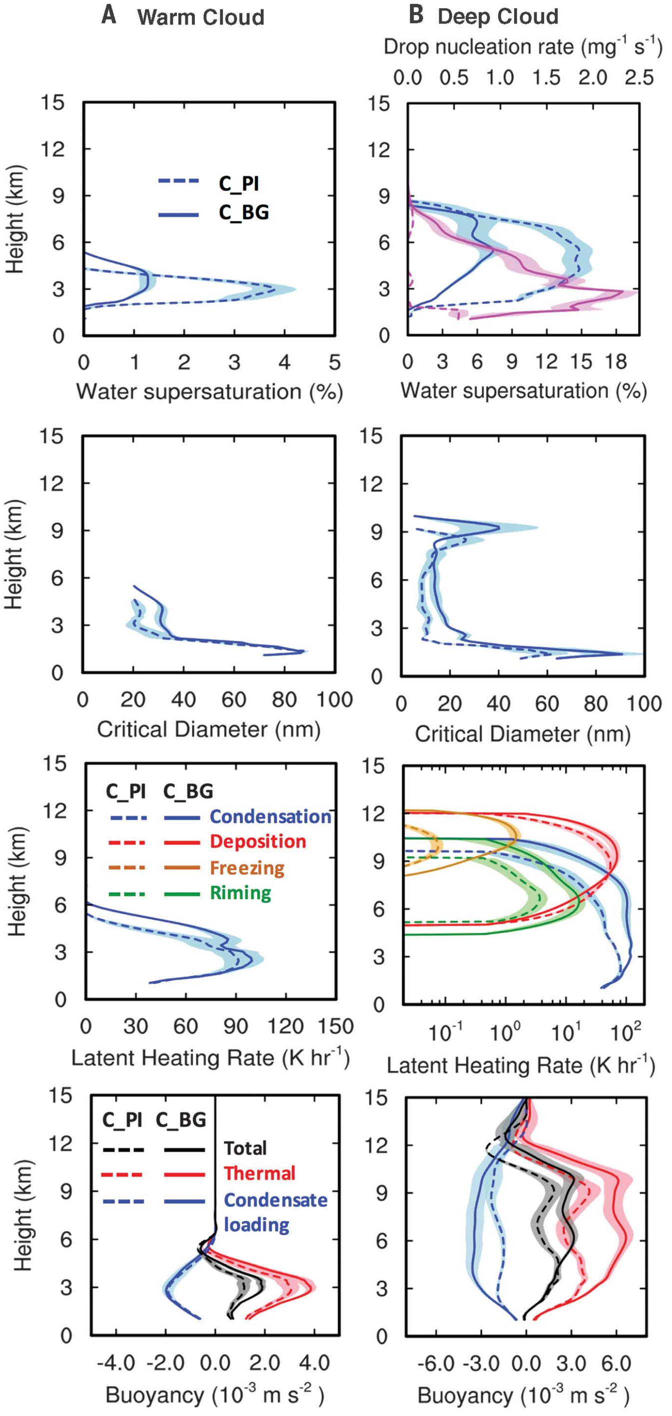

Fig. 4. Analysis of thermodynamics and microphysics. (**A** and **B**) Vertical profiles for the warm cloud (A) and deep cloud (B) from C_PI (dashed curves) and C_BG (solid curves). From top to bottom: water supersaturation; critical diameter for activation; latent heating from condensation (blue), deposition (red), drop freezing (orange), and riming (green); and buoyancy terms. The dashed and solid pink curves in the top panel of (B) show droplet nucleation rates from C_PI and C_BG, respectively (upper *x* axis). The thermal buoyancy includes contributions from both temperature and water vapor variations. The values for the warm cloud are averaged over the top 10 percentiles (i.e., 90th to 100th) of the updrafts with $w > 1$ m s^{-1} from a 30-min duration after the warm rain starts and the rain rate exceeds 0.5 mm hour^{-1} for the convective clouds in the red box in fig. S8. The values for the deep cloud are averaged over the top 10 percentiles (i.e., 90th to 100th) of the updrafts with $w > 2$ m s^{-1} from a 30-min duration with 15 min before and after the strongest convection. Therefore, the specific time for the warm- and deep-cloud periods varies by simulation because of the time shift of convective clouds between the simulations. Shaded areas represent the standard error of the data.

effects than the “cold-phase invigoration” previously proposed (*13*). UAP$_{<50}$ increase the rainwater amount mainly through enhanced accretion of added cloud droplets and added graupel melting. Added UAP$_{<50}$ do not affect the timing of precipitation because UAP$_{<50}$ can be activated to form additional cloud droplets only after warm rain begins. In contrast, CCN$_{>50}$ suppress and delay warm rain and then delay peak precipitation.

The large magnitude of the condensation effects is likely a result of the very warm, moist, and clean conditions in the Amazon wet season. This leads to a mechanism different from that associated with dry-season events over the Amazon [i.e., cold-phase invigoration (*13*, *22–24*)] or other dryer or colder locations [e.g., (*11*, *42*, *43*)]. A key factor is the ample cloud droplet coalescence in the tropical rainforest environment that is not affected by human activities. This coalescence rapidly removes droplets; droplet removal leads to suppressed condensation, leaving a high supersaturation for activating UAP$_{<50}$. This is corroborated by sensitivity tests with droplet collision-coalescence processes shut off for both background (C_BG) and plume-affected (P3_BG) cases, which show small differences in water supersaturation between the two cases, in contrast to the large differences when droplet collision-coalescence processes occur.

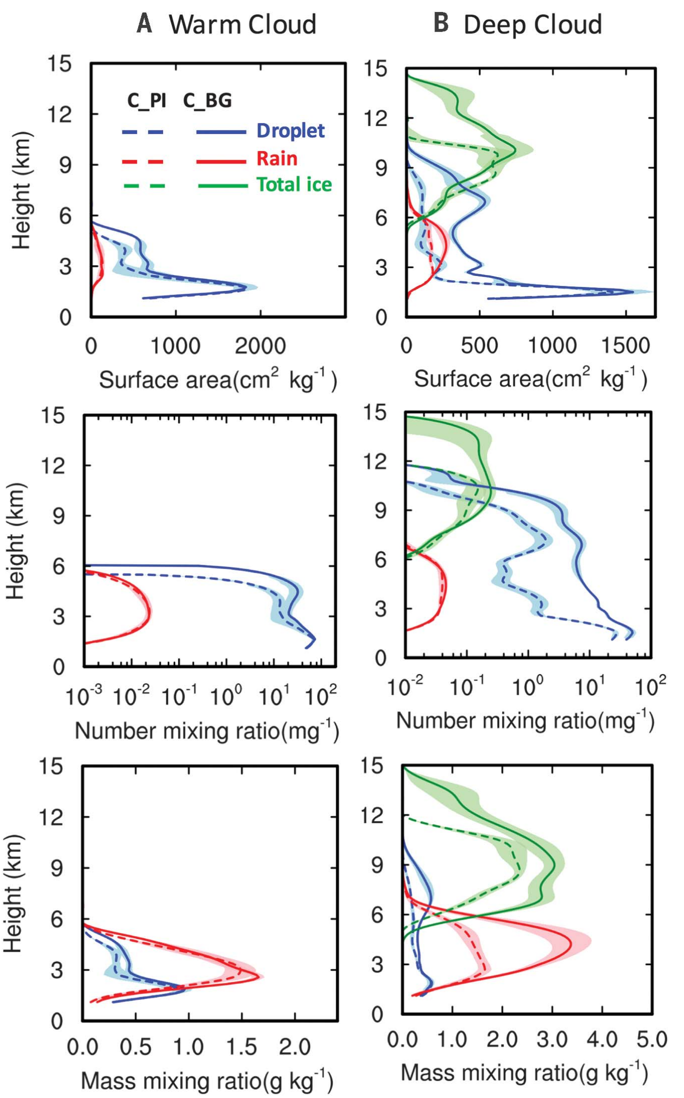

Fig. 5. Additional microphysical properties. (**A** and **B**) Analogous to Fig. 4, showing vertical profiles for droplet surface area (top), droplet number (middle), and mass mixing ratios (bottom) for cloud droplets (blue), rain drops (red), and ice-phase particles (green). The ice-phase particles include cloud ice, snow, and graupel. Shaded areas represent the standard error of the data.

It has been believed that there is a cutoff size—typically larger than 60 nm (*20*)—for aerosol particles to be able to serve as CCN for a specific region or typical aerosol type (*18*). Generally, UAP$_{<50}$ are not considered to contribute to CCN because their small sizes require high supersaturation. Our findings show that under the present-day Manaus regional background, approximated PI, and present-day pristine environments over the Amazon region, UAP$_{<50}$ can effectively serve as CCN for droplet nucleation well above the cloud base after coalescence starts. DCCs in the natural rainforest environment over the Amazon, where fine particles are scarce, may be especially susceptible to the addition of UAP$_{<50}$, as shown by this work. The dearth of new particle formation in the Amazon boundary layer under natural conditions might be a result of low sulfuric acid concentration; another possible reason is that the products of gas-phase oxidation of isoprene do not facilitate new particle formation as efficiently as those from oxidation of other biogenic volatile organic compounds (e.g., monoterpenes). However, anthropogenic emissions in this region may induce aerosol nucleation and produce a large amount of UAP$_{<50}$ through various mechanisms (*44*, *45*); for instance, interactions of anthropogenic sulfur and NO$_x$ with biogenic sources such as organic acids from aromatics enhance aerosol nucleation.

A recent study showed that aerosol concentrations over the Amazon peak at the upper troposphere (*46*), unlike the VD assumed in our model simulations. We conducted sensitivity tests (*34*) by using a VD similar to that in figure 7B of (*46*). Similar convective invigoration by increasing UAP$_{<50}$ through the same mechanism is seen (fig. S15, A and B). The new VD does not affect the conclusion because the maximum supersaturation peaks at an altitude of 6 km and the latent heating at low levels is the major contributor to convection intensification, so the addition of UAP$_{<50}$ at upper levels would not greatly affect the convective invigoration below it. However, the new VD causes stronger convective invigoration at upper levels because of higher aerosol concentrations. Another uncertainty results from the aerosol SD assumed in the simulation. We also carried out sensitivity tests by using a SD measured by a fast integrated mobility spectrometer [FIMS (*47*)] on aircraft at ~20 km downwind from Manaus (*34*). The results were similar to the previous simulations with a different SD (fig. S15, C and D). Thus, we infer that any aerosol scenario that contains a large ratio of UAP$_{<50}$ to CCN$_{>50}$ in a humid environment would produce the UAP$_{<50}$ effects we report in this study.

Because all UAP$_{<50}$ are removed in our simulations for examining the UAP$_{<50}$ effects, and because small numbers of UAP$_{<50}$ are observed at the remote rainforest site in the central Amazon Basin [e.g., figure 6A of (*39*)], we conducted an additional sensitivity test, C_PI2, in which UAP$_{<50}$ (60 cm^{-3}) were added to C_PI (Table 1) (*34*). We found that the differences in updraft velocity and supersaturation between C_PI and C_PI2 are very small (fig. S16, A and B). Thus, our conclusion and the proposed mechanism are not affected by the small amount of UAP$_{<50}$ in the PI condition. This indicates that we should expect similarly large UAP$_{<50}$ effects for pristine regions with low UAP$_{<50}$ concentration. The intrusion of urban areas such as the Manaus metropolis produces a large amount of UAP$_{<50}$, which may drastically change convective and precipitation conditions over the Amazon Basin by producing stronger convective clouds and precipitation.

All of our tests with different aerosol properties (SD and VD) indicate that observed and simulated UAP$_{<50}$ effects and the proposed mechanism are robust. Given the importance of the Amazon Basin in global circulation and hydrology, the ultrafine pollution particles introduced by human activities could have profound effects on other places around the globe. A lack of aerosol nucleation (or a low concentration of ultrafine particles) and the existence of ample moisture may not be unique to the Amazon Basin and may also occur in other tropical forests and oceans, further highlighting the global importance of our results. For example, a recent study found a conspicuous enhancement of lightning over shipping lanes in the equatorial Indian Ocean (*48*). We conclude that UAP$_{<50}$ can modulate convection and rain-forming processes more strongly than previously considered, especially in pristine regions. Therefore, the changes

Table 1. Model simulations. Abbreviations: BG, present-day background aerosol condition in the Manaus region; PI, preindustrial aerosol condition; P3, factor of 3 increase in N_a for plume; C, clean condition (i.e., no plume); L in PL3, large aerosol particles (i.e., $D > 50$ nm). Peaked refers to a measured size distribution that has a peak value over a size range; upper-level peak refers to a measured vertical distribution with aerosols peaked at upper levels (*34*). N/A means that no plume is applied (i.e., aerosols are horizontally uniform over the domain at the model initial time).

Simulation	Acronym	Size distribution	Vertical distribution	Hygroscopicity (κ)	N_a of domain (per cubic centimeter)		N_a of Manaus pollution plume (per cubic centimeter)	
					$CCN_{>50}$	$UAP_{<50}$	$CCN_{>50}$	$UAP_{<50}$
Manaus regional background with pollution plume	P3_BG	Power law + peaked	Exponential decrease	0.12	130	820	390	2460
Manaus regional background	C_BG	Power law + peaked	Exponential decrease	0.12	130	820	N/A	N/A
PI condition without $UAP_{<50}$	C_PI	Peaked	Exponential decrease	0.12	130	0	N/A	N/A
Sensitivity test for P3_BG without $UAP_{<50}$	PL3_PI	Peaked	Exponential decrease	0.12	130	0	390	0
Sensitivity test for VD based on C_BG	C_BG_VD	Power law + peaked	Upper-level peak	0.12	130	820	N/A	N/A
Sensitivity test for VD based on C_PI	C_PI_VD	Peaked	Upper-level peak	0.12	130	0	N/A	N/A
Sensitivity test for SD based on P3_BG	P3_BG_SD	Peaked	Exponential decrease	0.12	450	3350	1350	10,050
Sensitivity test for SD based on C_BG	C_BG_SD	Peaked	Exponential decrease	0.12	450	3350	N/A	N/A
Sensitivity test for SD based on C_PI	C_PI_SD	Peaked	Exponential decrease	0.12	450	0	N/A	N/A
PI condition with $UAP_{<50}$	C_PI2	Peaked	Exponential decrease	0.12	130	60	N/A	N/A
Sensitivity test for C_PI with mean ATTO	C_PI_ATTO	Peaked	Exponential decrease	0.12	200	0	N/A	N/A
Sensitivity test for C_BG with $CCN_{>50}$ from mean ATTO	C_BG_ATTO	Peaked	Exponential decrease	0.12	200	820	N/A	N/A

of ultrafine pollution particles from preindustrial conditions to the present may possibly have appreciably changed deep convective clouds.

REFERENCES AND NOTES

1. R. A. Houze Jr., *Cloud Dynamics* (Elsevier/Academic Press, ed. 2, 2014).
2. H. C. Barnes, R. A. Houze Jr., *J. Geophys. Res. Atmos.* **121**, 8269–8296 (2016).
3. *Climate Change 2013: The Physical Science Basis. Contribution of Working Group I to the Fifth Assessment Report of the Intergovernmental Panel on Climate Change* (Cambridge Univ. Press, 2013).
4. J. Fan, Y. Wang, D. Rosenfeld, X. Liu, *J. Atmos. Sci.* **73**, 4221–4252 (2016).
5. W. K. Tao, J. P. Chen, Z. Li, C. Wang, C. Zhang, *Rev. Geophys.* **50**, RG2001 (2012).
6. A. P. Khain, *Environ. Res. Lett.* **4**, 015004 (2009).
7. S. S. Lee, L. J. Donner, V. T. J. Phillips, Y. Ming, *J. Geophys. Res.* **113**, D16202 (2008).
8. Z. J. Lebo, J. H. Seinfeld, *Atmos. Chem. Phys.* **11**, 5407–5429 (2011).
9. R. L. Storer, S. C. van den Heever, *J. Atmos. Sci.* **70**, 430–446 (2013).
10. S. C. van den Heever, G. L. Stephens, N. B. Wood, *J. Atmos. Sci.* **68**, 699–718 (2011).
11. Z. Li *et al.*, *Nat. Geosci.* **4**, 888–894 (2011).
12. X. Yang, Z. Li, *J. Geophys. Res. Atmos.* **119**, 1835–1844 (2014).
13. D. Rosenfeld *et al.*, *Science* **321**, 1309–1313 (2008).
14. A. P. Khain, V. Phillips, N. Benmoshe, A. Pokrovsky, *J. Atmos. Sci.* **69**, 2787–2807 (2012).
15. Q. Chen *et al.*, *Atmos. Chem. Phys.* **17**, 9585–9598 (2017).
16. J. Fan *et al.*, *Proc. Natl. Acad. Sci. U.S.A.* **110**, E4581–E4590 (2013).
17. U. Pöschl *et al.*, *Science* **329**, 1513–1516 (2010).
18. M. O. Andreae, *Science* **315**, 50–51 (2007).
19. S. T. Martin *et al.*, *Atmos. Chem. Phys.* **10**, 11415–11438 (2010).
20. U. Lohmann, J. Feichter, *Atmos. Chem. Phys.* **5**, 715–737 (2005).
21. I. Koren, G. Dagan, O. Altaratz, *Science* **344**, 1143–1146 (2014).
22. M. O. Andreae *et al.*, *Science* **303**, 1337–1342 (2004).
23. I. Koren, J. V. Martins, L. A. Remer, H. Afargan, *Science* **321**, 946–949 (2008).
24. J. C. Lin, T. Matsui, R. A. Pielke Sr., C. Kummerow, *J. Geophys. Res.* **111**, D19204 (2006).
25. J. C. Zhou, E. Swietlicki, H. C. Hansson, P. Artaxo, *J. Geophys. Res.* **107**, 8055 (2002).
26. M. Kulmala *et al.*, *Atmos. Chem. Phys.* **11**, 13061–13143 (2011).
27. J. Wang *et al.*, *Nature* **539**, 416–419 (2016).
28. M. Pikridas *et al.*, *Atmos. Chem. Phys.* **15**, 10219–10237 (2015).
29. S. T. Martin *et al.*, *Bull. Am. Meteorol. Soc.* **98**, 981–997 (2017).
30. S. T. Martin *et al.*, *Atmos. Chem. Phys.* **16**, 4785–4797 (2016).
31. S. E. Giangrande *et al.*, *J. Appl. Meteorol. Climatol.* **52**, 2278–2295 (2013).
32. S. E. Giangrande *et al.*, *J. Geophys. Res. Atmos.* **121**, 12891–12913 (2016).
33. S. Tang *et al.*, *Atmos. Chem. Phys.* **16**, 14249–14264 (2016).
34. See supplementary materials.
35. J. A. Marengo *et al.*, *Atmos. Chem. Phys. Discuss.* 10.5194/acp-2017-22 (2017).
36. A. P. Khain, A. Pokrovsky, M. Pinsky, A. Seifert, V. Phillips, *J. Atmos. Sci.* **61**, 2963–2982 (2004).
37. J. Fan *et al.*, *J. Geophys. Res.* **117**, D00K36 (2012).
38. W. C. Skamarock *et al.*, *A Description of the Advanced Research WRF Version 3* (National Center for Atmospheric Research, 2008).
39. M. L. Pöhlker *et al.*, *Atmos. Chem. Phys. Discuss.* 10.5194/acp-2017-847 (2017).
40. M. L. Pöhlker *et al.*, *Atmos. Chem. Phys.* **16**, 15709–15740 (2016).
41. M. A. Cecchini *et al.*, *Atmos. Chem. Phys.* **16**, 7029–7041 (2016).
42. R. Zhang, G. Li, J. Fan, D. L. Wu, M. J. Molina, *Proc. Natl. Acad. Sci. U.S.A.* **104**, 5295–5299 (2007).
43. Y. Wang *et al.*, *Proc. Natl. Acad. Sci. U.S.A.* **111**, 6894–6899 (2014).
44. R. Zhang, A. Khalizov, L. Wang, M. Hu, W. Xu, *Chem. Rev.* **112**, 1957–2011 (2012).
45. M. Shrivastava *et al.*, *Rev. Geophys.* **55**, 509–559 (2017).
46. M. O. Andreae *et al.*, *Atmos. Chem. Phys. Discuss.* 10.5194/acp-2017-694 (2017).
47. J. Wang, M. Pikridas, S. R. Spielman, T. Pinterich, *J. Aerosol Sci.* **108**, 44–55 (2017).
48. J. A. Thornton, K. S. Virts, R. H. Holzworth, T. P. Mitchell, *Geophys. Res. Lett.* **44**, 9102–9111 (2017).

ACKNOWLEDGMENTS

This study was supported by the U.S. DOE, Office of Science, Atmospheric System Research Program. The Pacific Northwest National Laboratory (PNNL) is operated for DOE by Battelle Memorial Institute under contract DE-AC06-76RLO1830. This research used PNNL Institutional Computing resources. Y.Z. and Z.L. were supported by NSF grant AGS1534670 and National Science Foundation of China grant 91544217. D.R. was supported by project BACCHUS European Commission FP7-603445. S.E.G. represents Brookhaven Science Associates LLC under DOE contract DE-SC0012704. The DOE Atmospheric Radiation Measurement (ARM) Climate Research Facility's

GoAmazon field campaign data were used. The x-band and s-band (SIPAM) radar data were supported by the CHUVA project. We thank the GoAmazon team and the CHUVA team for their effort to produce the observational data. We acknowledge support from the Central Office of the Large Scale Biosphere Atmosphere Experiment in Amazonia (LBA), Instituto Nacional de Pesquisas da Amazonia (INPA), Universidade do Estado do Amazonas (UEA), and the local Research Foundation (FAPEAM). L.A.T.M., P.A., and H.M.J.B. were supported by FAPESP grants 2009/15235-8, 2013/05014-0, and 2013/50510-5. The work was conducted under authorization 001030/2012-4 of the Brazilian National Council for Scientific and Technological Development (CNPq). For the operation of the ATTO site, we acknowledge support by the German Federal Ministry of Education and Research (BMBF contract 01LB1001A), the Brazilian Ministério da Ciência, Tecnologia e Inovação (MCTI/FINEP contract 01.11.01248.00), and the Amazon State University (UEA), FAPEAM, LBA/INPA, and SDS/CEUC/RDS-Uatumã. We thank C. Schumacher and A. Funk at Texas A&M University for the SIPAM data, T. Biscaro for the x-band data, S. Tang at Lawrence Livermore National Laboratory for the input of local convective system selection, S. Hagos at PNNL for the input of model configuration, and C. Kuang at Brookhaven National Laboratory for help in understanding the uncertainty of Scanning Mobility Particle Sizer data. The observational data including x-band and SIPAM radar data from CHUVA can be obtained from DOE ARM data archive www.archive.arm.gov/discovery/#v/results/s/fiop::amf2014goamazon, which is available to the community. The model simulation data are archived at PNNL PIC and are available at https://dtn2.pnl.gov/data/jiwen/GoAmazon_simulations_sci/.

SUPPLEMENTARY MATERIALS

www.sciencemag.org/content/359/6374/411/suppl/DC1
Materials and Methods
Supplementary Text
Figs. S1 to S17
Table S1
References (*49*–*53*)

26 May 2017; accepted 22 December 2017
10.1126/science.aan8461